Inverse topological insulator with tunable intersurface coupling

Matthew Brahlek[1†], Nikesh Koirala[1†], Jianpeng Liu[1], Tahir I. Yusufaly[1], Maryam Salehi[2], Myung-Geun Han[3], Yimei Zhu[3], David Vanderbilt[1], and Seongshik Oh[1,*]

[1]Department of Physics & Astronomy, Rutgers, The State University of New Jersey, Piscataway, New Jersey 08854, U.S.A.

[2]Department of Materials Science and Engineering, Rutgers, The State University of New Jersey, Piscataway, New Jersey 08854, U.S.A.

[3]Condensed Matter Physics & Materials Science, Brookhaven National Lab, Upton, NY 11973, U.S.A.

*Correspondence should be addressed to ohsean@physics.rutgers.edu

[†]These authors contributed equally to this work

Abstract: **Massless, Diraclike topological surface states (TSS) form at the interface between materials that belong to different topological classes (topological insulator (TI), and non-TI), and have been realized in systems where a single slab of TI is surrounded by a non-TI (vacuum or any non-TI). Here, we extend the notion of a topological description of electronic materials and introduce the inverse topological insulator (ITI) system by sandwiching a layer of the tunable non-TI $(Bi_{1-x}In_x)_2Se_3$ (band gap 0 ~ 1.3 eV) between two layers of the prototypical TI Bi_2Se_3. In conventional single slab TIs, the bulk state is most often conducting, which allows deleterious coupling of the TSS. In contrast, the $(Bi_{1-x}In_x)_2Se_3$ barrier layer in the ITI system is a reliable and tunable insulator, which allows the bulk state between the TSS to be varied from metallic to truly insulating state. On this new platform, we show how the interfacial TSS emerge and become decoupled as the band gap and thickness of the non-TI layer was systematically changed. This ITI paradigm will open new routes to realize the novel properties and applications of topological materials.**

The topological classification scheme is rooted in the ability to distill the global properties of an object down into a single number known as a topological invariant. This notion of topology can be extended from the archetypal example of geometric topology, where shapes are classified based solely on the number of holes, to electronic materials, where the main physical implication occurs on the boundary between materials that belong to different topological classes. In the 3-dimensional (3D) class of TIs, unusual topological surface states (TSS) form on the 2-dimensional (2D) boundary with non-TIs. These surface states have metallic gapless energy bands, which disperse linearly with momentum like massless photons, and the spins of the surface electrons are locked perpendicular to the direction of their momentum (see Refs. (*1*-*2*)). Since the initial discovery, experimental confirmation of these novel properties has largely been confined to surface-sensitive probes such as angle-resolved photo emission spectroscopy (*3*-*5*) and scanning tunneling microscopy (*6*); direct transport measurements of the TSS have proven difficult due to the intrinsic defects that pin the Fermi level into either the conduction or valence bands, which effectively shorts the transport through the TSS (*7*-*16*).

Figure 1A shows the typical experimental and theoretical framework that has been used to study TIs, which consists of a single slab of a TI (topological invariant of 1) surrounded by a non-TI (topological invariant of 0), and it is at this interface that the TSS are formed. Here we present a new platform to study the topological nature of materials by inverting the single-slab archetype and surrounding a non-TI by a TI. The bulk-boundary correspondence (BBC) theorem(*1*) maintains that this inverse topological insulator (ITI) geometry is physically equivalent to the standard TI geometry because the TSS formed at such an interface are nominally identical, which can be seen by comparing Fig. 1A and B. Through the use of molecular beam epitaxy (MBE), Fig. 2C shows that this ITI geometry is feasible by inserting a layer of the tunable non-TI $(Bi_{1-x}In_x)_2Se_3$ (band gap ~1.3 eV at x = 100% (*17*-*20*)) between two layers of the TI Bi_2Se_3 (*21*). By varying the thickness of the non-TI barrier layer from the ultra-thin (1 quintuple layer, 1 QL ≈ 1 nm) to the thick regime (> 100 QL), we find that the Bi_2Se_3 layers become electrically isolated and the TSS emerge at the interfaces when the In_2Se_3 thickness is above ~3 QL, as shown by both transport measurements and first-principles calculations. Further, by decreasing x in the

$(Bi_{1-x}In_x)_2Se_3$ barrier layer from x = 100% to 30%, its potential barrier height is lowered, and the coupling strength gradually increases for the same layer thickness. For a fixed composition x, the interfacial TSS undergoes a coupled-to-decoupled transition as the thickness grows beyond a critical value. This transition from coupled to decoupled can be described by a simple analytic function of the thickness and composition, which suggests the presence of a fundamental mechanism behind the intersurface coupling through this true band-insulating barrier layer. However, when x is reduced below ~25%, the barrier layer becomes metallic and TSS remain fully coupled over the entire thickness range, with the analytical function breaking down.

The weak anti-localization (WAL) effect is a common feature of the magneto-resistance in TI thin films (see Fig. 2A for measurement geometry, and note that both layers of Bi_2Se_3 are equally contacted when the In wires are physically pressed into the film) (*10, 12-13, 15-16, 22-25*). The WAL effect is typically seen as a sharp cusp at small field in resistance vs magnetic field, and is quantifiable by the Hikami-Larkin-Nagaoka (HLN) formula $\Delta G(B) = \tilde{A}e^2/(2\pi h)(ln[\hbar/(4el_\phi^2 B)] - \Psi[1/2 + \hbar/(4el_\phi^2 B)])$, where h is Planck's constant, Ψ is the digamma function, $\tilde{A}$ is related to the number of 2D conducting channels ($\tilde{A} \approx 1$ for each channel), and l_ϕ is the de-phasing length (*26*). In general l_ϕ is limited by the inelastic scattering length, which depends strongly on microscopic details such as disorder and phonons. In contrast, $\tilde{A}$ has been found to be much more robust, and monitoring the effective channel number gives information about the coupling between the various transport channels (*12-13, 15-16, 22*). In TIs, $\tilde{A} \approx 1$ occurs when the bulk state is conducting and the surface-to-bulk scattering time is shorter than the electron dephasing time; in this limit electrons are allowed to scatter from the surface into the bulk before losing their phase information (*15, 22, 25, 27*). Most TI films, including the Bi_2Se_3 films studied here, have conducting bulk states and thus exhibit $\tilde{A} \approx 1$ over a wide thickness range from 2 to above 100 QL (*12-13*).

Introducing a variable-thickness In_2Se_3 layer in the center of a 60-QL Bi_2Se_3 slab induces an $\tilde{A}$ = $1 \rightarrow 2$ transition with increasing In_2Se_3 thickness, as shown in Fig. 2B. Due to the large band gap of

In_2Se_3, ~1.3 eV compared with ~0.3 eV for Bi_2Se_3, $\tilde{A}$ indicates the existence of two channels even at a thickness of only ~3 QL; this indicates that the transport properties of the top and bottom Bi_2Se_3 layers are electrically isolated for barrier thicknesses of ~3 QL or more, indirectly implying the emergence of TSS at the interfaces. Fig. 2C shows an extension of this experiment where another unit of Bi_2Se_3-In_2Se_3 has been added (Bi_2Se_3-In_2Se_3-Bi_2Se_3-In_2Se_3-Bi_2Se_3 with corresponding thicknesses of 30-20-30-*t*-30 QL); $\tilde{A}$ responds by transitioning from $2 \rightarrow 3$ with increasing In_2Se_3 thickness *t*, which confirms the counting nature of the channel interpretation of $\tilde{A}$ observed in Bi_2Se_3 with insulating bulk states (*15-16*, *25*).

To understand the microscopic origin of the emergence of the TSS near the transitional region, we carried out first-principles calculations based on density-functional theory (DFT). We first performed calculations on bulk Bi_2Se_3 and In_2Se_3, which were extended to Bi_2Se_3-In_2Se_3 supercells by allowing the construction of Wannierized effective Hamiltonians (see supplementary materials for more details). Figure 2D shows the band gap at the Γ point near the interface of Bi_2Se_3-In_2Se_3, and confirms that the gapless nature of the TSS is attained with increasing In_2Se_3 thickness. The spatial electronic properties can be further seen by tracking the real space density of the states around the Fermi level (RDOS, see Ref. (*28*) and supplementary materials), as shown in Figs. 2E-H. This calculation shows that the RDOS increases near the Bi_2Se_3-In_2Se_3 interface even for a single QL of In_2Se_3, indicating a new state has begun to emerge. By 2-3 QL of In_2Se_3, the RDOS splits, peaking near the Bi_2Se_3-In_2Se_3 interfaces and diminishing near the center, which implies the formation of the TSS at the interfaces and development of an insulating bulk in the middle of In_2Se_3. The finite density of states in the In_2Se_3 region is due to the evanescent decay of the TSS wave functions into the In_2Se_3 layer, and extends around ~2 QL into the In_2Se_3 layer, which is better seen for the relatively thick 8QL In_2Se_3 in Fig. 2H. This shows that the emergence of the TSS from the DFT calculation is consistent with the WAL $\tilde{A} = 1 \rightarrow 2$ transition, both of which suggest that the two Bi_2Se_3 layers are fully isolated beyond ~3 QL of In_2Se_3 in between.

It was previously shown that $(Bi_{1-x}In_x)_2Se_3$ undergoes compositional dependant topological and metal-insulator phase transitions: It first undergoes a TI to non-TI transition near $x \approx$ 3-7% (*18-20*), then

transitions into a weakly insulating variable-range-hopping state near $x \approx 15\%$ and finally into a strong band insulator for $x > 25\%$ (*18*). Using this, we can explore the $\tilde{A} = 1 \rightarrow 2$ transition by systematically decreasing x in the $(Bi_{1-x}In_x)_2Se_3$ layer which lowers the potential height of the barrier. Plots of $\tilde{A}$ versus $(Bi_{1-x}In_x)_2Se_3$ thickness are presented in Figs. 3A-C, which show that as x decreases from 40 to 30 and to 20%, the transition region is pushed to larger thickness.

These behaviors can be understood by applying an extremely simple quantum-mechanical tunneling model as follows. We think of the electrons in the individual Bi_2Se_3 layers as nearly free electrons due to the metallic states there, as illustrated in Fig. 3D, and since the barrier layer of $(Bi_{1-x}In_x)_2Se_3$ is insulating, it can be thought of analogously as a potential barrier. The tunneling through this barrier will be described by a transmission coefficient T. If this tunneling is negligible, T will be zero, and the top and bottom metallic layers of Bi_2Se_3 will be decoupled from each other, leading to two WAL channels ($\tilde{A} = 2$). In the opposite limit, $T = 1$, the top and bottom Bi_2Se_3 layers will be strongly coupled and will act as a unit, leading to just one WAL channel ($\tilde{A} = 1$). The simplest way to connect these end points is through a linear approximation, $\tilde{A}(T) = 2 - T$ and using the standard quantum-mechanical form $T = 1/(1 + e^{2(t-t_0)/l_0})$ for free-electron tunneling through a square barrier, we obtain $\tilde{A}(t) = 2 - 1/(1 + e^{2(t-t_0)/l_0})$. This function, which is parameterized by the critical transition thickness t_0 and the transition width l_0, shows good agreement with the experimental data, which can be seen by comparing the experimental data to the fits in Fig. 2B-C and Fig. 3A-C.

We have plotted the values of the fitting parameters t_0 and l_0 in Fig. 3E-F, and it can be seen that for $x \gtrsim 30\%$, both t_0 and l_0 are almost exactly exponential functions of x. The consistency of this trend implies that the barrier's electronic properties are described by the tunneling model in this composition range. However, the exponential dependence breaks down below $x = 30\%$. To quantify this analytic behavior, we fit the experimental data to $t_0(x) = \tau e^{-x/x_0}$ and $l_0(x) = \lambda\, e^{-x/x_0}$, which results in $\tau \approx 90$ nm, $\lambda \approx 60$ nm, and both t_0 and l_0 consistently yield $x_0 \approx 25\%$, which coincides with the composition where the exponential trend breaks down. In order to see this more clearly, we generated the red dotted

curve for x = 20% in Fig. 3C by extrapolating the exponential behavior to x = 20% (see the red stars in Fig. 3E-F); this curve clearly deviates from the experimental data for x = 20%. This indicates that below x ≈ 25%, the insulating behavior of $(Bi_{1-x}In_x)_2Se_3$ fully breaks down, giving way to a metallic regime. This composition coincides with the point where the band-insulating state dies out in homogeneous $(Bi_{1-x}In_x)_2Se_3$ films (*18*).

This transition can be understood from the band-alignment diagrams in Fig. 3G generated by DFT calculations for Bi_2Se_3 and $(Bi_{1-x}In_x)_2Se_3$ with x = 20, 60 and 100%. What is noticeable is that the bottom of the conduction band for the barrier layer is clearly above that of Bi_2Se_3 for x = 60 and 100%, while for x = 20% the conduction band of barrier layer drops below that of Bi_2Se_3. If the Bi_2Se_3 crystals were perfect without any selenium vacancies, their Fermi levels ($E_{F,Ideal}$) would be at the Dirac point in the middle of the band gap. Then, the barrier would remain insulating all the way down and the band gap of the barrier would close at the topological phase transition near x ≈ 3-7%, so that x = 20% would behave as an insulating barrier like x = 60 and 100%. However, in practice, real Bi_2Se_3 layers have their Fermi levels ($E_{F,Real}$) slightly above the conduction band minimum, so that x = 20% behaves as a metal instead of an insulator. This analysis is fully consistent with the breakdown of the tunneling behavior for x below ~25% discussed above.

Figure 4A-C shows how $\tilde{A}$ changes with x for different barrier thicknesses (10, 20 and 30 QL). For each thickness, $\tilde{A}$ transitions from 1 to 2 with increasing x. If the empirical exponential relations hold between t_0 and x, and between l_0 and x, then there should be enough information to generate a curve that fits these data points. Using $\tilde{A}(t) = 2 - \frac{1}{1+e^{2(t-t_0)/l_0}} \rightarrow \tilde{A}(t,x) = 2 - \frac{1}{1+e^{2(t-t_0(x))/l_0(x)}}$, $l_0(x) \approx 60e^{-x/25}$ and $t_0(x) \approx 90e^{-x/25}$ (the numerical values were obtained above) allows the generation of the curves for $\tilde{A}$ vs x (for greater than ~25%) with *no free parameters*. The solid red curves in Fig. 4A-C agree well with the experimental data for x > 25%, and this further confirms that the exponential relations for l_0 and t_0 hold for all x greater than ~25%.

Figure 4D summarizes the analytic behavior of $\tilde{A}$ as a function of thickness t and composition x, and Fig. 4E sketches how the coupling between the TSS evolves with the barrier layer properties. The well-defined behavior of $\tilde{A}$ with both x and t suggests presence of a fundamental mechanism underlying here. However, the exponential dependence of t_0 and l_0 on x is anomalous because Vegard's law predicts that the lattice parameters and band gap of an alloy should, to first order, interpolate linearly between the end members (*29*), which would manifest itself as a power-law, not an exponential, change in both t_0 and l_0. Further studies will be required to resolve the origin behind this effect.

In conclusion, by utilizing the ITI system, we have shown that the number of channels contributing to the WAL effect directly depends on the coupling strength through the barrier layer. When the barrier layer is metallic, the two surfaces behave as one channel; this mimics the standard TI material, whose bulk states are metallic, thus causing only one WAL channel to appear. When the barrier layer is insulating, the two surfaces act either as one or two WAL channels depending on the barrier height and thickness. This exemplifies how the ideal TSS with fully insulating bulk states should behave and corroborates recent experiments on TI films showing the $\tilde{A} = 1 \rightarrow 2$ transition with film thickness (*15-16*). Beyond this, the ITI system provides a unique platform for probing buried topological surface states with tunable bulk properties. We anticipate that this ITI paradigm will provide new pathways to TI-based nanostructures, thereby initiating further discoveries and applications.

Acknowledgements

This work is supported by ONR (N000141210456) and NSF (DMR-0845464, DMR-1005838, and DMREF-1233349). The work at Brookhaven National Lab is supported by U.S. Department of Energy, Office of Basic Energy Science, Division of Materials Science and Engineering, under Contract number DE-AC02-98CH10886. We acknowledge J. Garlow for TEM sample preparation using focused-ion beam at Center for Functional Nanomaterials, Brookhaven National Lab.

References

1. M. Z. Hasan, C. L. Kane, *Rev. Mod. Phys.* **82**, 3045 (2010).
2. X.-L. Qi, S.-C. Zhang, *Rev. Mod. Phys.* **83**, 1057 (2011).
3. D. Hsieh *et al.*, *Nature* **452**, 970 (2008).
4. Y. L. Chen *et al.*, *Science* **325**, 178 (2009).
5. Y. Xia *et al.*, *Nat. Phys.* **5**, 398 (2009).
6. P. Roushan *et al.*, *Nature* **460**, 1106 (2009).
7. J. G. Analytis *et al.*, *Nat. Phys.* **6**, 960 (2010).
8. N. P. Butch *et al.*, *Phys. Rev. B* **81**, 241301 (2010).
9. H. Steinberg, D. R. Gardner, Y. S. Lee, P. Jarillo-Herrero, *Nano Letters* **10**, 5032 (2010).
10. M. Liu *et al.*, *Phys. Rev. B* **83**, 165440 (2011).
11. J. G. Checkelsky, Y. S. Hor, R. J. Cava, N. P. Ong, *Phys. Rev. Lett.* **106**, 196801 (2011).
12. Y. S. Kim *et al.*, *Phys. Rev. B* **84**, 073109 (2011).
13. N. Bansal, Y. S. Kim, M. Brahlek, E. Edrey, S. Oh, *Phys. Rev. Lett.* **109**, 116804 (2012).
14. D. Kim *et al.*, *Nat. Phys.* **8**, 459 (2012).
15. D. Kim, P. Syers, N. P. Butch, J. Paglione, M. S. Fuhrer, *Nat. Commun.* **4**, 2040 (2013).
16. M. Brahlek, N. Koirala, M. Salehi, N. Bansal, S. Oh, *Phys. Rev. Lett.* **113**, 026801 (2014).
17. Y. Watanabe, S. Kaneko, H. Kawazoe, M. Yamane, *Phys. Rev. B* **40**, 3133 (1989).
18. M. Brahlek *et al.*, *Phys. Rev. Lett.* **109**, 186403 (2012).
19. L. Wu *et al.*, *Nat. Phys.* **9**, 410 (2013).
20. J. Liu, D. Vanderbilt, *Phys. Rev. B* **88**, 224202 (2013).
21. Z. Y. Wang *et al.*, *App. Phys. Lett.* **99**, 023112 (2011).
22. H. Steinberg, J. B. Laloë, V. Fatemi, J. S. Moodera, P. Jarillo-Herrero, *Phys. Rev. B* **84**, 233101 (2011).
23. J. Chen *et al.*, *Phys. Rev. B* **83**, 241304 (2011).
24. J. J. Cha *et al.*, *Nano Letters* **12**, 1107 (2012).
25. M. Brahlek, N. Koirala, N. Bansal, S. Oh, *ArXiv* **1408.1614**, (2014).
26. S. Hikami, A. I. Larkin, N. Nagaoka, *Prog. Theor. Phys.* **63**, 707 (1980).
27. H.-Z. Lu, S.-Q. Shen, *Phys. Rev. B* **84**, 125138 (2011).
28. Q. Zhang, Z. Zhang, Z. Zhu, U. Schwingenschlögl, Y. Cui, *ACS Nano* **6**, 2345 (2012).
29. A. R. Denton, N. W. Ashcroft, *Physical Review A* **43**, 3161 (1991).

Figure Captions

Fig. 1 (**A-B**) Topological surface states form when there is a change in topological invariant (v) across an interface (*i.e.* Δv = 1). (A) Typical experimental paradigm: a topological material (characterized by a topological invariant v_{TI} = 1) surrounded by non-topological insulator (v_{nTI} = 0), which forms a metallic topological surface state at the interface (indicated by the arrows). (**B**) Inverse topological insulator (ITI) is formed by inverting the role of non-TI and the topological material, and a nominally identical surface state forms at this interface. (**C**) High-resolution high-angle annular dark-field scanning transmission electron microscopy image showing the physical realization of the ITI geometry (B) in a Bi_2Se_3-In_2Se_3-Bi_2Se_3 heterostructure.

Fig. 2 (**A**) Schematic of the experimental setup where the films were grown on square substrates, and all layers of Bi_2Se_3 were contacted by pressed indium wires in the Van der Pauw geometry. (**B-C**) $\tilde{A}$ extracted from the HLN formula plotted versus thickness of the In_2Se_3 layer in Bi_2Se_3-In_2Se_3-Bi_2Se_3 (30-*t*-30 QL) (B), and Bi_2Se_3-In_2Se_3-Bi_2Se_3-In_2Se_3-Bi_2Se_3 (30-20-30-*t*-30 QL) (C). (**D**) Calculations of the energy gap at the interface of Bi_2Se_3-In_2Se_3 at the Γ point showing that the gap at the Dirac point closes as the In_2Se_3 thickness increases. (**E-F**) Schematic of the heterostructure formed for increasing In_2Se_3 thickness alongside the calculated real space density of the states (RDOS) around the Fermi level as a function of thickness, showing the emergence of the TSS at ~3 QL.

Fig. 3 (**A-C**) Thickness dependence of $\tilde{A}$ for Bi_2Se_3-$(Bi_{1-x}In_x)_2Se_3$-Bi_2Se_3 (30-*t*-30 QL) with x = 40, 30, and 20%, respectively. Symbols are experimental data, and the solid lines are the fits to the semi-empirical function (see text, and D). In (C) the solid line is the best fit to the data, while the red dotted line is the curve generated by extrapolating the exponential trend from the parameters shown as stars in E-F. (**D**) Schematic showing how the Bi_2Se_3-$(Bi_{1-x}In_x)_2Se_3$-Bi_2Se_3 structure can be thought of as a simple quantum-mechanical barrier separating the metallic states in Bi_2Se_3. Within this framework, it can be seen that tunneling increases as the barrier thickness is decreased or the height is lowered, thus accounting for

the observed behavior of $\tilde{A}$. (**E-F**) Compositional dependence of the fitting parameters extracted from the curves in (A-C) and Fig. 2B. Here t_0 (E) gives the critical thickness for the $\tilde{A} = 1 \rightarrow 2$ transition versus thickness, while l_0 (F) is the width of the transition region. The solid lines in (E) and (F) are exponential fits. The red stars are extrapolated parameters for x = 20%. Below $x \approx 25\%$ the data deviate from the exponential trend, consistent with an insulator-to-metal transition of the barrier layer. (**G**) Energy bands alignment of Bi_2Se_3-$(Bi_{1-x}In_x)_2Se_3$-Bi_2Se_3 for x = 20, 60 and 100% respectively. For $x \gtrsim 25\%$ the conduction band minimum of $(Bi_{1-x}In_x)_2Se_3$ is above the experimental (real) Fermi level $E_{F,Real}$, which makes the barrier layer insulating, while for $x \lesssim 25\%$ the conduction band minimum drops below $E_{F,Real}$, which makes the barrier metallic: with ideal Fermi levels ($E_{F,Ideal}$), the barrier should remain insulating even for x = 20%.

Fig. 4 (**A-C**) Compositional dependence of $\tilde{A}$ with the $(Bi_{1-x}In_x)_2Se_3$ barrier thickness fixed at 10, 20, and 30 QL respectively. The solid red lines for each thickness were generated by using the semi-empirical function for $x > 25\%$, with the x dependence given by the analytic relations for l_0 and t_0 vs. x in Fig. 3E-F, *with no free parameters*; this confirms that the exponential behavior holds for all $x > 25\%$. (**D**) Contour plot of the semi-empirical function for $\tilde{A}$ as a function of x and t for $x \gtrsim 25\%$; below $x \approx 25\%$, we took $\tilde{A}$ to be 1 due to the metallic nature of the barrier in this regime. The red dashed lines are cuts at constant thickness, which correspond to the solid red lines plotted in A-C. (**E**) Schematic showing the coupling ($\tilde{A}$ = 1, left) and decoupling ($\tilde{A}$ = 2, right) of the TSS across the $(Bi_{1-x}In_x)_2Se_3$ barrier layer.

Fig. 1 (double column)

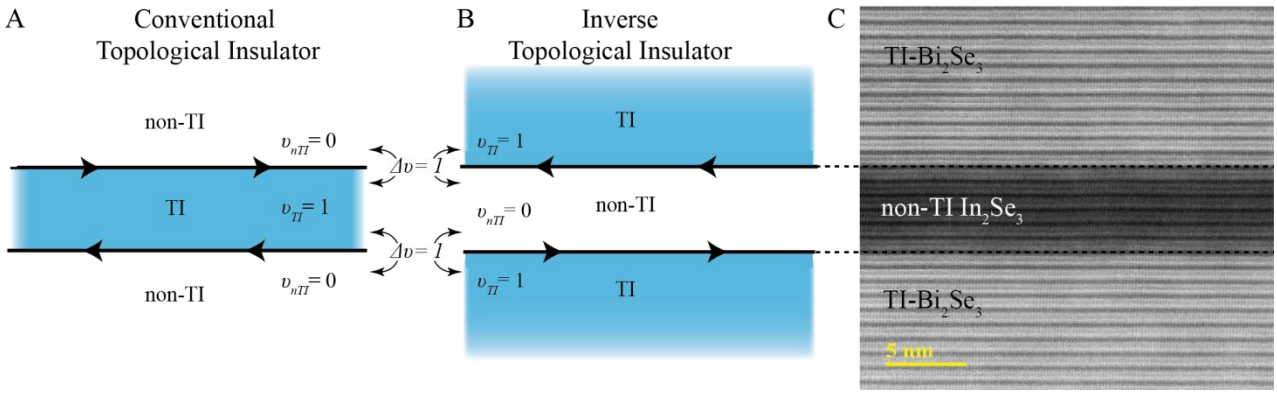

Fig. 2 (double column)

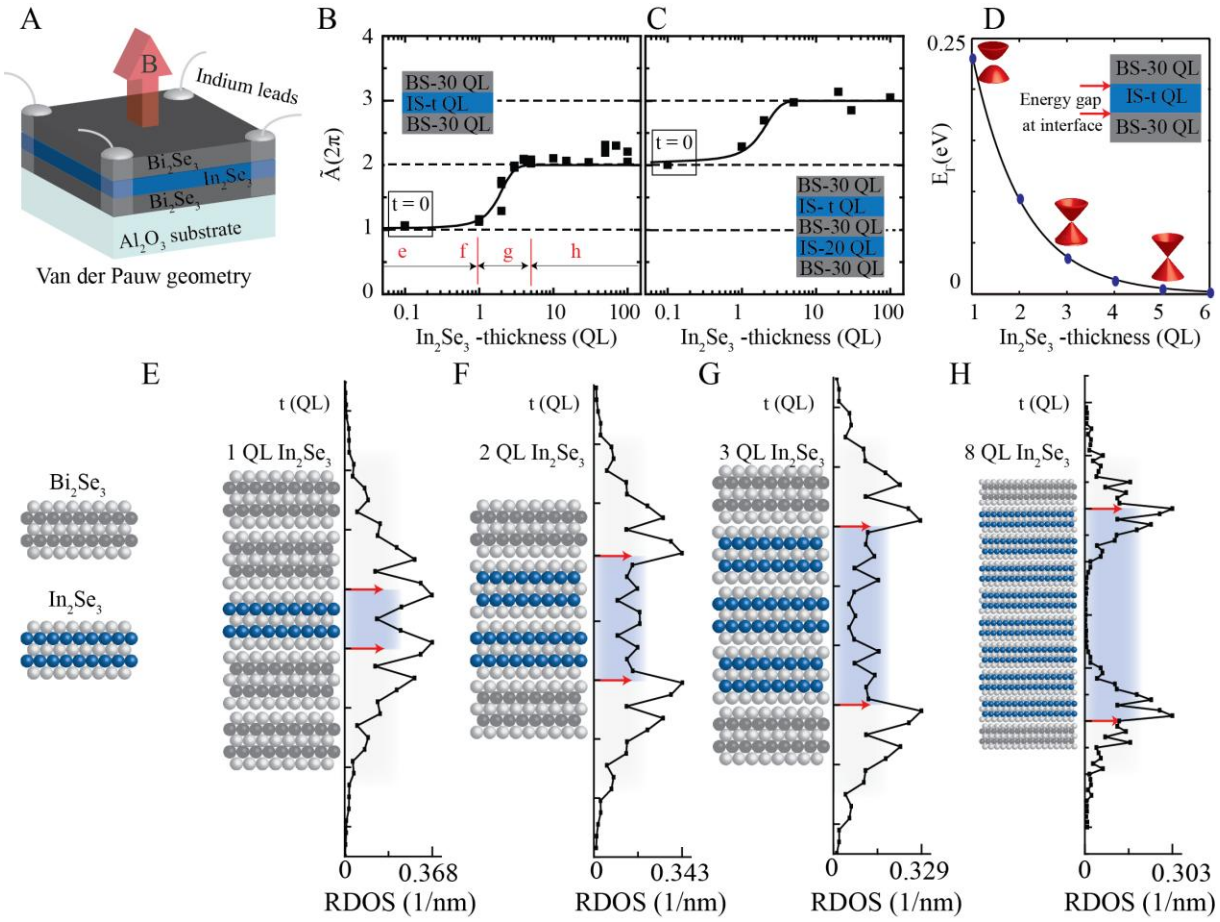

Fig. 3 (double column)

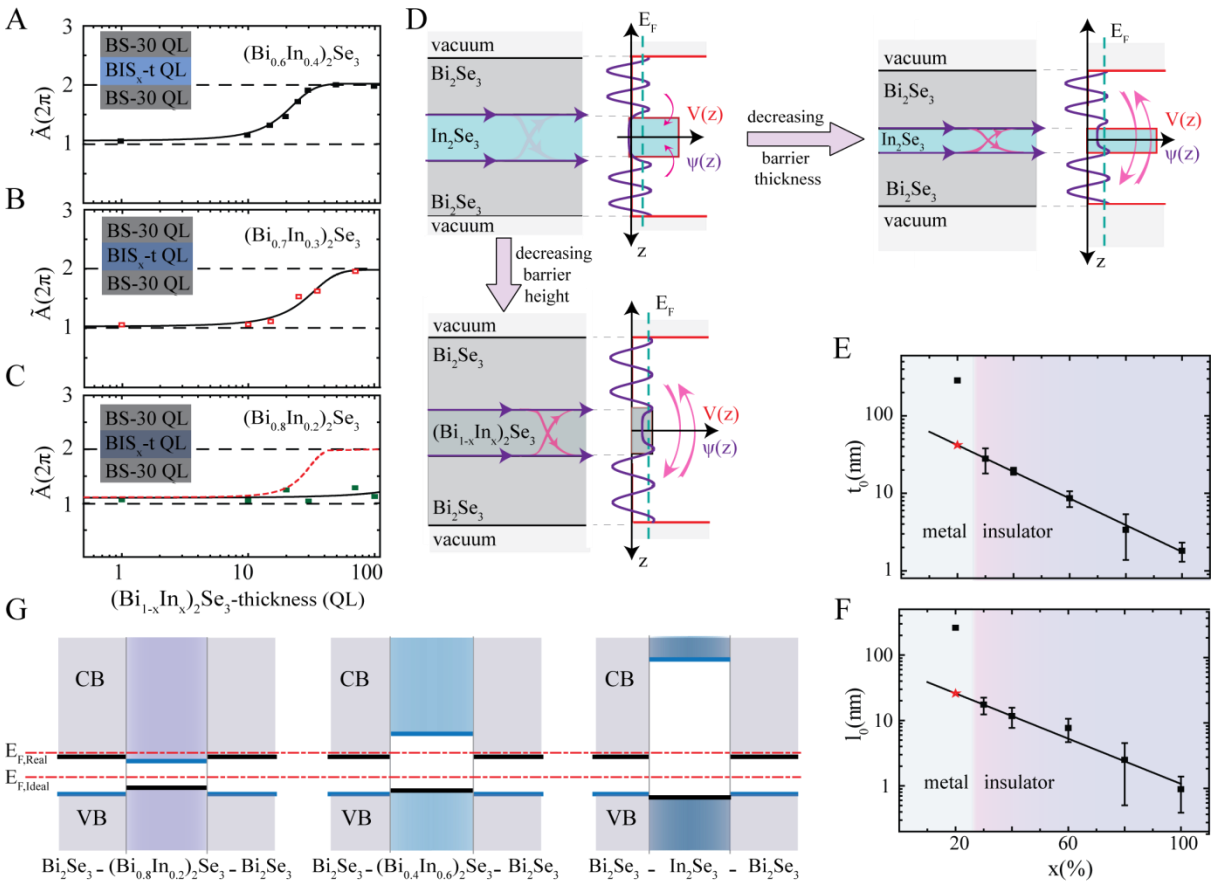

Fig. 4 (single column)